

PROBING WHIM AROUND GALAXY CLUSTERS WITH FAST RADIO BURSTS AND THE SUNYAEV-ZEL'DOVICH EFFECT

YUTAKA FUJITA

Theoretical Astrophysics, Department of Earth and Space Science, Graduate School of Science, Osaka University, 1-1
 Machikaneyama-cho, Toyonaka, Osaka 560-0043, Japan

TAKUYA AKAHORI

Graduate School of Science and Engineering, Kagoshima University, Kagoshima 890-0065, Japan

KEIICHI UMETSU

Institute of Astronomy and Astrophysics, Academia Sinica, P. O. Box 23-141, Taipei 10617, Taiwan

CRAIG L. SARAZIN

Department of Astronomy, University of Virginia, P.O. Box 400325, Charlottesville, VA 22904-4325, USA

KA-WAH WONG¹

Eureka Scientific, Inc., 2452 Delmer Street Suite 100, Oakland, CA 94602-3017, USA

¹Department of Physics and Astronomy, Minnesota State University, Mankato, MN 56001, USA

ABSTRACT

We propose a new method to probe the Warm Hot Intergalactic Medium (WHIM) beyond the virial radius (R_{200}) of a cluster of galaxies, where X-ray observations are not easily achievable. In this method, we use dispersion measures (DMs) of Fast Radio Bursts (FRBs) that appear behind the cluster and the Sunyaev-Zel'dovich (SZ) effect towards the cluster. The DMs reflect the density of the intracluster medium (ICM) including the WHIM. If we observe a sufficient number of FRBs in the direction of the cluster, we can derive the density profile from the DMs. Similarly, we can derive the pressure profile from the SZ effect. By combining the density and the pressure profiles, the temperature profile can be obtained. Based on mock observations of nearby clusters, we find that the density of the WHIM can be determined even at $> 2 R_{200}$ from the cluster center when FRB observations with the Square Kilometre Array (SKA) become available. The temperature can be derived out to $r \sim 1.5 R_{200}$, and the radius is limited by the current sensitivity of SZ observations.

Keywords: galaxies: clusters: general — intergalactic medium — pulsars: general — methods: observational

1. INTRODUCTION

It has been predicted that a diffuse warm hot intergalactic medium (WHIM) at temperatures $T \sim 10^5\text{--}10^7$ K contains $\sim 50\%$ of the baryons in the universe at low redshifts (e.g. Cen & Ostriker 1999; Davé et al. 2001). Although a number of surveys have been conducted to constrain the WHIM (e.g. Nicastro et al. 2005; Takei et al. 2007; Fujita et al. 2008; Danforth & Shull 2008; Tripp et al. 2008), they have detected only a fraction of the predicted amount of the WHIM. Some of the WHIM is expected to exist in the outskirts of galaxy clusters. This WHIM gradually falls into the clusters and is heated at accretion shocks (e.g. Ryu et al. 2003). Thus, we can understand the process in which the WHIM turns into the hot intracluster medium (ICM) in the clusters by exploring the WHIM in this region. The outskirts of clusters have been investigated in X-rays especially with *Suzaku* (e.g. Fujita et al. 2008; Reiprich et al. 2009; George et al.

2009; Kawaharada et al. 2010; Hoshino et al. 2010; Akamatsu et al. 2011; Simionescu et al. 2011; Walker et al. 2012; Sato et al. 2012; Ichikawa et al. 2013; Wong et al. 2016, see a recent review by Reiprich et al. 2013). Many of these observations show that the entropy of the ICM in the outskirts of massive clusters is smaller than that predicted by numerical simulations (e.g. Voit et al. 2005 but see Eckert et al. 2013), which may indicate that the heating is less effective than expected (e.g. Wong & Sarazin 2009; Fujita et al. 2013). Unfortunately, the X-ray observations are limited to $r \lesssim R_{200}$, where R_{200} is the radius at which the cluster density is 200 times the critical density at that redshift and is often regarded as the virial radius of the cluster (e.g. Navarro et al. 1996). In order to understand the heating process, observations of the WHIM at $r \gtrsim R_{200}$ are crucial. Although the signatures of the (thermal) Sunyaev-Zel'dovich (SZ) effect (Sunyaev & Zeldovich 1972) have been detected at $r \gtrsim R_{200}$ for a number of clusters (Planck Collaboration et al. 2013b, 2015a,b), it gives us only the information on the pressure profiles, and the density and the temperature profiles are not obtained separately.

Fast Radio Bursts (FRBs) are bright, unresolved, millisecond signals. Although their origin is not clear, their large dispersion measures (DMs) suggest that they are extragalactic (Lorimer et al. 2007; Keane et al. 2012; Thornton et al. 2013; Spitler et al. 2014; Burke-Spolaor & Bannister 2014; Ravi et al. 2015; Petroff et al. 2015; Masui et al. 2015). It has been proposed that the DMs of transient objects such as gamma-ray bursts (GRBs) and FRBs can be used to probe the WHIM along the line of sight (Ioka 2003; Inoue 2004). In this study, we propose a new idea to explore the WHIM by combining the DMs of FRBs and the SZ effect. We show that this method will reveal the properties of the WHIM at $r \gtrsim R_{200}$ when observations of FRBs with the Square Kilometre Array (SKA) become available. We use $H_0 = 70 \text{ km s}^{-1} \text{ Mpc}^{-1}$, $\Omega_m = 0.3$, and $\Omega_\Lambda = 0.7$.

2. DISPERSION MEASURES OF FRBS

So far at least 17 FRBs have been identified, and a catalogue compiled from the published literature is available¹. Their DMs are $\sim 400\text{--}1600 \text{ cm}^{-3} \text{ pc}$. Although the values of the DMs may depend on the distance to the FRBs, we treat that as a random variable for simplicity. From the catalogue, we find that the average of the DMs is $\langle \text{DM} \rangle_{17} = 785 \text{ cm}^{-3} \text{ pc}$ and the square root of the unbiased variance is $\sigma_{\text{DM}17} = 289 \text{ cm}^{-3} \text{ pc}$.

In this study, we focus on nearby clusters ($z \lesssim 0.1$) and FRBs that appear behind them. Indeed, the observed large DMs suggests cosmological origins at high redshifts of $z = 0.5\text{--}1$ (e.g. Akahori et al. 2016). If the FRBs have a redshift distribution similar to that for GRBs, the contribution of foreground FRBs can be ignored (e.g. Coward et al. 2013). Even if the foreground FRBs (and FRBs residing physically inside the cluster) cannot be ignored, SKA will be able to identify the host galaxies of the FRBs with its excellent resolution (Macquart et al. 2014). Once the hosts are identified, the determination of their redshifts will be possible. The DM of a single FRB measured by an observer is

$$\text{DM} = \int \frac{n_e}{1+z} dL, \quad (1)$$

where n_e is the electron density and z is the redshift of the gas (e.g. equation (4) in Deng & Zhang 2014). The integration is performed along the line of sight. The DM in the direction of a cluster should consist of

$$\text{DM}_c = \text{DM}_{\text{FRB}} + \text{DM}_{\text{IGM}} + \text{DM}_{\text{ICM}} + \text{DM}_{\text{MW}}, \quad (2)$$

where DM_{FRB} , DM_{IGM} , DM_{ICM} , and DM_{MW} are DM contributions from the FRB (and the surrounding medium), the intergalactic medium (IGM), the ICM, and the Milky Way Galaxy, respectively. From now on, the term ICM includes the WHIM in the higher than normal density region around the cluster, unless otherwise mentioned. Moreover, we represent the average of multiple DMs by “ $\langle \rangle$ ”. The average $\langle \text{DM} \rangle_c$ should be larger than the average when there is no DM contribution from the ICM:

$$\langle \text{DM} \rangle_{\text{nc}} = \langle \text{DM} \rangle_{\text{FRB}} + \langle \text{DM} \rangle_{\text{IGM}} + \langle \text{DM} \rangle_{\text{MW}}. \quad (3)$$

Note that while the extragalactic contribution, $\langle \text{DM} \rangle_{\text{FRB}} + \langle \text{DM} \rangle_{\text{IGM}}$, may be independent of the direction to the FRB, $\langle \text{DM} \rangle_{\text{MW}}$ may be dependent on direction, because the column density of the interstellar medium (ISM) of the Milky Way Galaxy varies. In that case, we can use the FRBs that are detected around the cluster of interest to determine the local value of $\langle \text{DM} \rangle_{\text{MW}}$. Above the Galactic plane, we have estimated that a variation of DM_{MW} in even a huge field of 900 deg^2 centered on the Virgo or the Coma cluster is only $\sim 6 \text{ cm}^{-3} \text{ pc}$ based on a simple Milky Way model by Akahori et al. (2013). Thus, we ignore the Milky Way variation. In the SKA era, $\langle \text{DM} \rangle_{\text{MW}}$ would have been well-modeled by observing numerous pulsars and its dependence on the direction would have been determined

¹ <http://astronomy.swin.edu.au/pulsar/frbcat/>

(Han et al. 2014), although we cannot know about the electron density beyond those pulsars and the ISM may be too structured to be covered by those pulsars especially in the direction of the Galactic plane. We further assume that the 17 FRBs are not affected by the ICM since the fraction of the sky covered by rich clusters is small. Thus, we assume that $\langle \text{DM} \rangle_{\text{nc}} \sim \langle \text{DM} \rangle_{17}$ and the intrinsic dispersion is $\sigma_{\text{DM}}^2 = \sigma_{\text{DM}17}^2$.

In order to derive the properties of the ICM, we have to determine $\langle \text{DM} \rangle_{\text{ICM}}$. From equation (1), the DM contribution from the ICM is

$$\text{DM}_{\text{ICM}} = \int_{-\infty}^{\infty} \frac{n_{\text{ICM}}}{1+z} dL, \quad (4)$$

where n_{ICM} is the electron density of the cluster. For the outskirts of a nearby cluster, it is expected to be

$$\text{DM}_{\text{ICM}} \sim 200 \text{ cm}^{-3} \text{ pc} \left(\frac{n_e}{1 \times 10^{-4} \text{ cm}^{-3}} \right) \left(\frac{L_c}{2 \text{ Mpc}} \right), \quad (5)$$

where L_c is the size of the cluster. This DM is comparable to $\sigma_{\text{DM}} \sim 289 \text{ cm}^{-3} \text{ pc}$, which means that the DM variation of FRBs cannot be ignored when we estimate DM_{ICM} ². Since

$$\langle \text{DM} \rangle_{\text{ICM}} = \langle \text{DM} \rangle_c - \langle \text{DM} \rangle_{\text{nc}} \quad (6)$$

(equations (2) and (3)), we need to measure both $\langle \text{DM} \rangle_c$ and $\langle \text{DM} \rangle_{\text{nc}}$. We can obtain the former by observing FRBs that appear behind the cluster and averaging their DMs. The latter can be determined by assuming that $\langle \text{DM} \rangle_{\text{nc}}$ equals the average DM of FRBs observed outside clusters (not behind clusters) or $\langle \text{DM} \rangle_{\text{out}}$. The error is given by $\delta \langle \text{DM} \rangle_{\text{out}} = \sigma_{\text{DM}} / \sqrt{N_{\text{out}}}$, where N_{out} is the number of FRBs observed there. If we take a sufficiently wide region outside a cluster, we expect that $\langle \text{DM} \rangle_{\text{out}}$ is determined with a negligible error, because SKA will detect enormous number of FRBs ($N_{\text{out}} \gg 1$) and $\delta \langle \text{DM} \rangle_{\text{out}} = \sigma_{\text{DM}} / \sqrt{N_{\text{out}}} \rightarrow 0$. Thus, we can precisely derive $\langle \text{DM} \rangle_{\text{nc}} (= \langle \text{DM} \rangle_{\text{out}})$.

Now we can estimate $\langle \text{DM} \rangle_{\text{ICM}}$ from $\langle \text{DM} \rangle_c$ and $\langle \text{DM} \rangle_{\text{nc}}$ using equation (6). However, if we attempt to derive $\langle \text{DM} \rangle_{\text{ICM}}$ for a narrow region in a cluster projected on the sky, the number of FRBs observed there, N_{in} , can be relatively small, which may cause an error. The error of $\langle \text{DM} \rangle_{\text{ICM}}$ depends on those of $\langle \text{DM} \rangle_c$ and $\langle \text{DM} \rangle_{\text{nc}}$. While the latter can be ignored because $\delta \langle \text{DM} \rangle_{\text{nc}} = \delta \langle \text{DM} \rangle_{\text{out}} \approx 0$, the former is written as

$$\delta \langle \text{DM} \rangle_c^2 = \delta \langle \text{DM} \rangle_{\text{ICM,int}}^2 + \delta \langle \text{DM} \rangle_{\text{nc,in}}^2. \quad (7)$$

While $\langle \text{DM} \rangle_{\text{ICM}}$ is not a directly observable quantity, its intrinsic uncertainty, $\delta \langle \text{DM} \rangle_{\text{ICM,int}}$, can be ignored because DM_{ICM} has nothing to do with the DM variation of FRBs or σ_{DM} . The error $\delta \langle \text{DM} \rangle_{\text{nc,in}}$ is the uncertainty of $\langle \text{DM} \rangle_{\text{nc}}$ that is for the FRBs *detected inside the narrow region*. Since $\delta \langle \text{DM} \rangle_{\text{nc,in}}$ is given by $\sigma_{\text{DM}} / \sqrt{N_{\text{in}}}$, it cannot be ignored if N_{in} is small. Thus, we obtain $\delta \langle \text{DM} \rangle_c = \delta \langle \text{DM} \rangle_{\text{nc,in}} = \sigma_{\text{DM}} / \sqrt{N_{\text{in}}}$ from equation (7). In summary, $\langle \text{DM} \rangle_{\text{ICM}}$ can be derived from equation (6) assuming that $\langle \text{DM} \rangle_{\text{nc}} = \langle \text{DM} \rangle_{\text{out}}$, and the error can be estimated by

$$\delta \langle \text{DM} \rangle_{\text{ICM}} = \delta \langle \text{DM} \rangle_c = \sigma_{\text{DM}} / \sqrt{N_{\text{in}}}. \quad (8)$$

In particular, if we consider one specific FRB ($N_{\text{in}} = 1$), the error is

$$\delta \langle \text{DM} \rangle_{\text{ICM}} = \sigma_{\text{DM}}. \quad (9)$$

From now on, we discuss $\langle \text{DM} \rangle_{\text{ICM}}$ rather than $\langle \text{DM} \rangle_c$, because $\langle \text{DM} \rangle_{\text{nc}}$ is just a constant, and we refer to $\langle \text{DM} \rangle_{\text{ICM}}$ as DM for simplicity.

3. MOCK OBSERVATIONS

3.1. Models

For mock observations, we construct a spherical model cluster based on observations of the Coma cluster ($z = 0.023$), because detailed SZ observations have been made for the Coma cluster. The radius of the cluster is $R_{200} = 2.62 \text{ Mpc}$ (Planck Collaboration et al. 2013b). The thermal SZ effect from the ICM is represented by the Compton y parameter:

$$y = \int_{-\infty}^{\infty} \sigma_{\text{T}} n_{\text{ICM}} \frac{k_{\text{B}} T_{\text{ICM}}}{m_e c^2} dL = \frac{\sigma_{\text{T}}}{m_e c^2} \int_{-\infty}^{\infty} P_{\text{ICM}} dL, \quad (10)$$

where σ_{T} is the Thomson cross section, k_{B} is the Boltzmann constant, n_{ICM} is the ICM electron density, T_{ICM} is the temperature, m_e is the electron mass, c is the speed of light, and $P_{\text{ICM}} \equiv n_{\text{ICM}} k_{\text{B}} T_{\text{ICM}}$ is the electron pressure. We

² On the other hand, observational errors of DMs for individual FRBs are much smaller than σ_{DM} and can be ignored (see <http://astronomy.swin.edu.au/pulsar/frbcat/>).

ignore the SZ effect other than the thermal SZ effect produced by the cluster. For the SZ effect, we choose *Planck* for the mock observations. The y parameter has been measured out to $\sim 1.5 R_{200}$ with *Planck*, and we adopt an ICM profile that reproduces the *Planck* observations (Planck Collaboration et al. 2013b). The density profile is

$$n_{\text{ICM}}^2(r) = n_0^2 \frac{(r/r_c)^{-\alpha}}{[1 + (r/r_c)^2]^{3\beta-\alpha/2}} \frac{1}{[1 + (r/r_s)^3]^{\epsilon/3}}, \quad (11)$$

where $n_0 = 2.9 \times 10^{-3} \text{ cm}^{-3}$, $r_c = 0.4 \text{ Mpc}$, $r_s = 0.7 \text{ Mpc}$, $\alpha = 0$, $\beta = 0.57$, and $\epsilon = 1.3$. The temperature profile is

$$T_{\text{ICM}}(r) = T_0 \frac{(r/r_c)^{-a}}{[1 + (r/r_t)^b]^{c/b}}, \quad (12)$$

where $T_0 = 6.9 \text{ keV}$, $r_t = 0.26 \text{ Mpc}$, $a = 0$, $b = 3.4$, and $c = 0.6$. The functional forms of equations (11) and (12) were proposed by Vikhlinin et al. (2006). Note that n_{ICM} and T_{ICM} are actually degenerate because *Planck* observed the y parameter that depends on P_{ICM} (equation (10)). We assume that equations (11) and (12) can be extrapolated over $\gtrsim 1.5 R_{200}$.

We consider mock observations of this model cluster with SKA1-MID, which is sensitive in the same radio band as the Parkes telescope that has detected most of the FRBs so far. At present, the estimated event rate of FRBs based on Parkes detections is $10_{-4}^{+6} \times 10^3 \text{ events sky}^{-1} \text{ day}^{-1}$ (Macquart et al. 2014) or $7_{-3}^{+5} \times 10^3 \text{ events sky}^{-1} \text{ day}^{-1}$ (Champion et al. 2016). Macquart et al. (2014) predicted that the detection rate would be ~ 200 times higher with SKA1-SUR. Since SKA1-SUR has been deferred, we make an estimation based on SKA1-MID, which has a sensitivity of a few times better than that of SKA1-SUR³. Assuming that SKA1-MID's detection rate is ~ 200 – 500 times larger than that of Parkes, the event rate is estimated to be $\sim 8 \times 10^5$ – $8 \times 10^6 \text{ events sky}^{-1} \text{ day}^{-1}$, which means $N_{\text{FRB}} \sim 0.8$ – $8 \text{ events deg}^{-2} \text{ hour}^{-1}$. So far, most FRBs have been detected with Parkes at 1.2–1.5 GHz. In this band, the field of view (FOV) of SKA1-MID is $S_{\text{FOV}} \sim 0.75 \text{ deg}^2$ at 1.4 GHz (Dewdney et al. 2016). Thus, we expect that the number of FRBs detected in the SKA's FOV is $N_{\text{FOV}} \sim S_{\text{FOV}} N_{\text{FRB}} \sim 0.6$ – $6 \text{ events hour}^{-1}$. The required exposure time in hours per FOV to detect FRBs at a rate of $n_{\text{SKA}} (\text{events deg}^{-2})$ is $T_{\text{exp}} = n_{\text{SKA}} / N_{\text{FRB}} = n_{\text{SKA}} / (N_{\text{FOV}} / S_{\text{FOV}})$. We can fairly easily achieve a detection rate of $n_{\text{SKA}} = 5$ – $20 \text{ events deg}^{-2}$ with a reasonable exposure time. For example, the required time is $T_{\text{exp}} \sim 0.6 \text{ hour}$ for $n_{\text{SKA}} = 5 \text{ events deg}^{-2}$ and $N_{\text{FOV}} = 6 \text{ events hour}^{-1}$, and $T_{\text{exp}} \sim 25 \text{ hours}$ for $n_{\text{SKA}} = 20 \text{ events deg}^{-2}$ and $N_{\text{FOV}} = 0.6 \text{ events hour}^{-1}$.

Since the apparent size of the Coma cluster may be too large ($\sim 54 \text{ deg}^2$ for $< 3 R_{200}$) to cover with SKA1-MID with a reasonable observation time, we consider a mock cluster located at $z = 0.07$ ($\sim 6.6 \text{ deg}^2$ for $< 3 R_{200}$), because massive clusters like the Coma cluster have been identified around that redshift (e.g. Reiprich & Böhringer 2002).

3.2. Results of Forward Modeling

We perform mock observations based on forward modeling, in which comparison between models and data is made in the data space (DM and y). The forward modeling is appropriate even when the S/N of observations is not particularly high. In the Appendix, we show the results of backward modeling (Abel transform), in which comparison is made in the model space (the ICM density, pressure, and temperature). Results of the forward and backward modelings should be consistent within the uncertainty if the S/N is large enough. The statistical errors are small enough that non-linear effects are not expected to bias the results. Thus, we ignore the systematic bias effects.

Using the ICM profile explained in the previous section, we construct mock DM data and y profiles. For the DM data, we focus on the region of $r_{\text{min}} = \theta_{\text{min}} d_A = 0.5 R_{200} < \theta d_A < r_{\text{max,DM}} = \theta_{\text{max,DM}} d_A = 6 R_{200}$, where θ is the angle from the cluster center, and d_A is the angular diameter distance to the cluster. For the y parameter, we consider the region of $r_{\text{min}} < \theta d_A < r_{\text{max,y}} = \theta_{\text{max,y}} d_A = 2 R_{200}$, because significant signals of the SZ effect have been detected at $\lesssim 2 R_{200}$ (Planck Collaboration et al. 2013a,b). Moreover, the influence of *Planck*'s beam convolution (FWHM = $10'$) can be ignored because $r_{\text{min}}/d_A = \theta_{\text{min}} \sim 30'$ is much larger than the FWHM.

We randomly distribute FRBs on the sky with $n_{\text{SKA}} = 20 \text{ events deg}^{-2}$. The input-model DM profile, $\text{DM}_{\text{ICM}}(\theta)$, can be obtained from equation (4). Following equation (9), the DMs of individual FRBs are randomly perturbed with a Gaussian distribution, with the dispersion determined by σ_{DM} . We note that the actual DMs may not have a Gaussian distribution especially when the difference of the DMs comes from the redshift of the FRBs. We obtained 10^3 different realizations in total. The result of one realization is shown in Fig. 1a. We then fit the DMs with a power-law:

$$\text{DM}_{\text{fit}}(\theta) = \text{DM}_{\text{fit},0} (\theta d_A / r_{\text{min}})^{-s}, \quad (13)$$

³ http://www.astron.nl/phiscc2014/Documents/Surveys/SKA_PHISCC_Braun.pdf

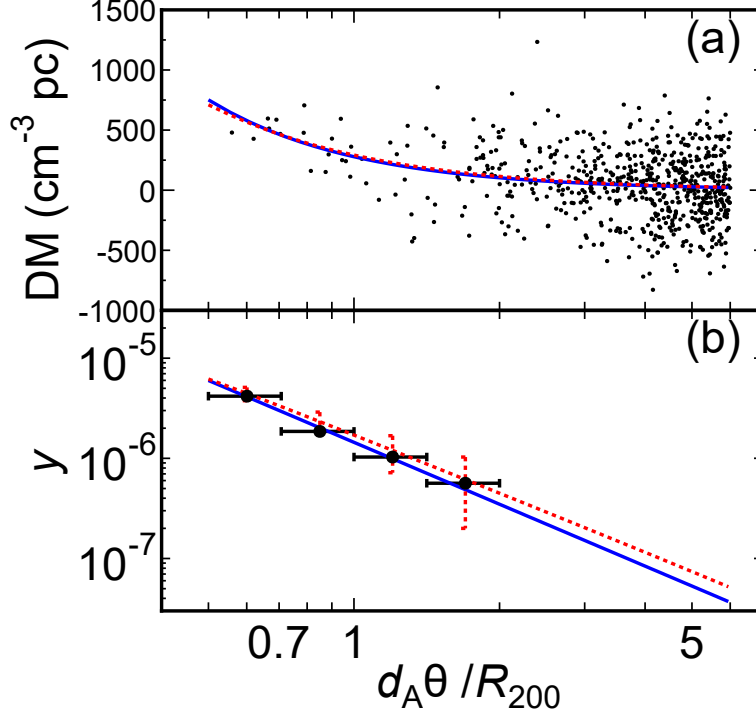


Figure 1. (a) Dots are a realization of simulated DMs with statistical errors when $n_{\text{SKA}} = 20 \text{ events deg}^{-2}$, and the solid blue line is the power-law fit. The dotted red line is the input-model DM profile, $\text{DM}_{\text{ICM}}(\theta)$. (b) Dots are a realization of simulated y parameters with statistical errors, and the solid blue line is the power-law fit. The dotted red line is the input-model y profile, $y(\theta)$. Vertical bars around the dotted line represent the 1σ uncertainty $\sigma_{y,i} = \sqrt{C_{ii}}$ at each radial bin.

where $\text{DM}_{\text{fit},0}$ and s are the parameters for the fit. The result of a fit and the input-model profile are shown in Fig. 1a. Since the obtained DM profile has a one-to-one relation to the density profile, it can be converted into the density profile by the Abel transform (equation (A3)):

$$n_{\text{ICM,fit}}(r) = \frac{\Gamma((1+s)/2)}{\sqrt{\pi} \Gamma(s/2)} \frac{\text{DM}_{\text{fit},0}(1+z)}{r_{\text{min}}} \left(\frac{r}{r_{\text{min}}} \right)^{-s-1}, \quad (14)$$

where Γ is the gamma function.

The input-model y profile, $y(\theta)$, is derived from equation (10) and is shown as the dotted line in Fig. 1b. In order to simulate mock *Planck* observations of the model cluster, we logarithmically divide the region $\theta_{\text{min}} < \theta < \theta_{\text{max},y}$ into four concentric annular bins ($N = 4$). The observed y value of the i -th radial bin ($i = 1, \dots, N$) is expressed as the linear sum of the bin-averaged y signal, $\langle y_i \rangle$, which can be estimated from equation (10), and the random noise contribution, δy_i .

$$y_i = \langle y_i \rangle + \delta y_i. \quad (15)$$

Here, δy_i ($i = 1, \dots, N$) is a noise vector drawn from a multivariate Gaussian distribution with mean zero and covariance $C_{ij} \equiv \langle \delta y_i \delta y_j \rangle$ ($i, j = 1, \dots, N$). We express the i -th diagonal element of the covariance matrix as $\sigma_{y,i} = \sqrt{C_{ii}}$, which is the rms noise level at the i -th bin. Noise realizations can be generated as follows: First, we model the covariance matrix C_{ij} in terms of the noise angular power spectrum $P_{\ell,\text{noise}}$ shown as MILCA-NILC98 F/L data in Fig. 11 of [Planck Collaboration et al. \(2015b\)](#), where ℓ represents the angular multiple. In analogy with equations (15) and (16) of [Umetsu et al. \(2011\)](#), the covariance matrix is given by

$$C_{ij} = \int \frac{\ell d\ell}{2\pi} P_{\ell,\text{noise}} \hat{J}_0(\ell\theta_i) \hat{J}_0(\ell\theta_j), \quad (16)$$

where θ_i is the representative angular radius of the i -th bin given by $y(\theta_i) = \langle y_i \rangle$, and \hat{J}_0 is the Bessel function of the first kind and order zero (J_0) that is averaged over the i -th bin (see equation (16) in [Umetsu et al. 2011](#)). Then we perform Cholesky decomposition of the $N \times N$ covariance matrix as $C = LL^T$, where L is an $N \times N$ lower triangular matrix. We assign a random noise fluctuation, δy_i , as in $\delta y_i = \sum_j L_{ij} \xi_j$, where ξ_j is a random number drawn from the Gaussian distribution with zero mean and unit variance (see section 6.1.2 of [Umetsu et al. 2010](#)). We show the

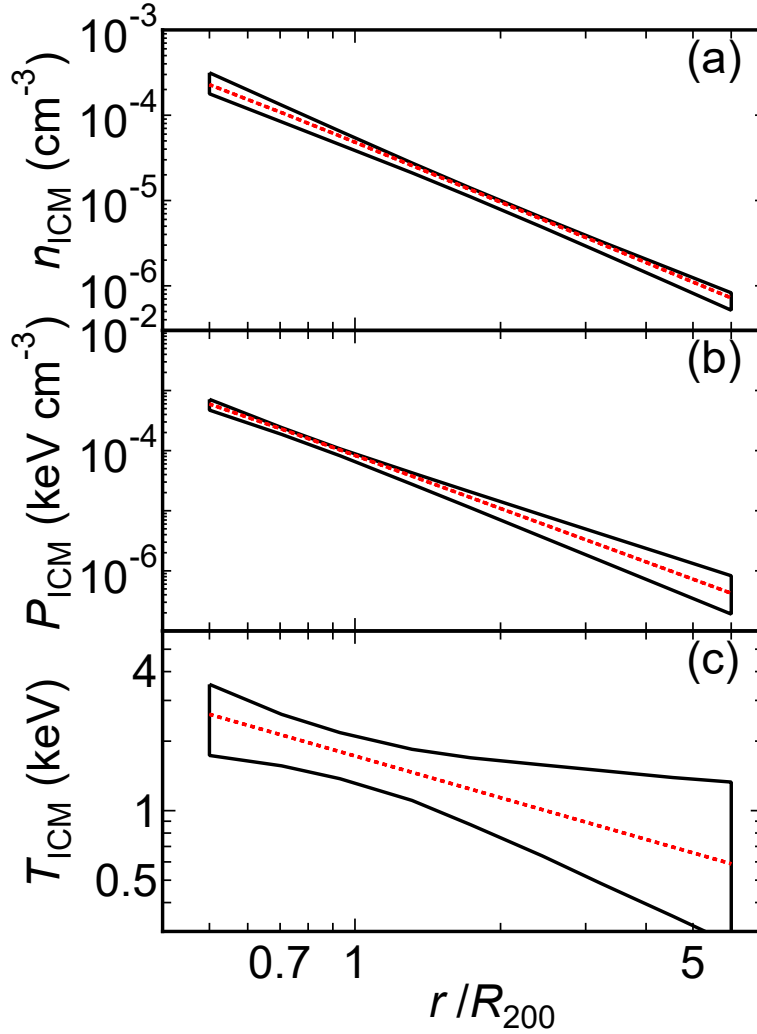


Figure 2. Solid ribbons are the reproduced profiles with 1σ errors for (a) ICM density (b) pressure, and (b) temperature when $n_{\text{SKA}} = 20 \text{ events deg}^{-2}$. Input-model profiles (equations (11) and (12)) are shown by dotted lines.

results of one realization in Fig. 1b. We fit y_i ($i = 1, \dots, N$) with a power-law:

$$y_{\text{fit}}(\theta) = y_{\text{fit},0}(\theta d_A / r_{\text{min}})^{-q}, \quad (17)$$

where $y_{\text{fit},0}$ and q are the parameters for the fit. The weight of the fit is $1/\sigma_{y,i}^2$. The result of a fit is shown as the solid line in Fig. 1b. As is the case with DM, the result of the fit can be converted into the pressure profile (equation (A5)):

$$P_{\text{ICM,fit}}(r) = \frac{\Gamma((1+q)/2)}{\sqrt{\pi} \Gamma(q/2)} \frac{\sigma_T}{m_e c^2} \frac{y_{\text{fit},0}}{r_{\text{min}}} \left(\frac{r}{r_{\text{min}}} \right)^{-q-1}. \quad (18)$$

From equations (14) and (18), we obtain the temperature profile $T_{\text{ICM,fit}}(r) = P_{\text{ICM,fit}}(r)/(k_B n_{\text{ICM,fit}}(r))$. From now on, we omit the suffix ‘fit’ unless otherwise mentioned.

From 10^3 Monte-Carlo realizations, we find the reduced χ^2 for the fit by equation (13) to lie in the range 0.94–1.05 (1σ) with degrees of freedom of ~ 650 , and that by equation (17) in the range 0.05–0.44 (1σ) with degrees of freedom of 2. Here we note that the small values of the latter are due to the strong correlation between different radial bins as estimated from the *Planck* y noise angular power spectrum. Note that while the input-model profiles are not power-laws (equations (11) and (12)), we fit them power-laws (equations (14) and (18)). However, the power-laws can approximate the input-model profiles sufficiently well in the cluster outskirts, and their differences contribute to the reduced χ^2 only by $\sim 3 \times 10^{-5}$ for the DM fit and by $\sim 6 \times 10^{-4}$ for the y fit.

At each radius r , we derive 1σ ranges of n_{ICM} , P_{ICM} , and T_{ICM} and show them in Fig. 2. The ICM density is determined out to $r \sim 6 R_{200}$, and the pressure and the temperature are determined out to $r \sim 4 R_{200}$ with

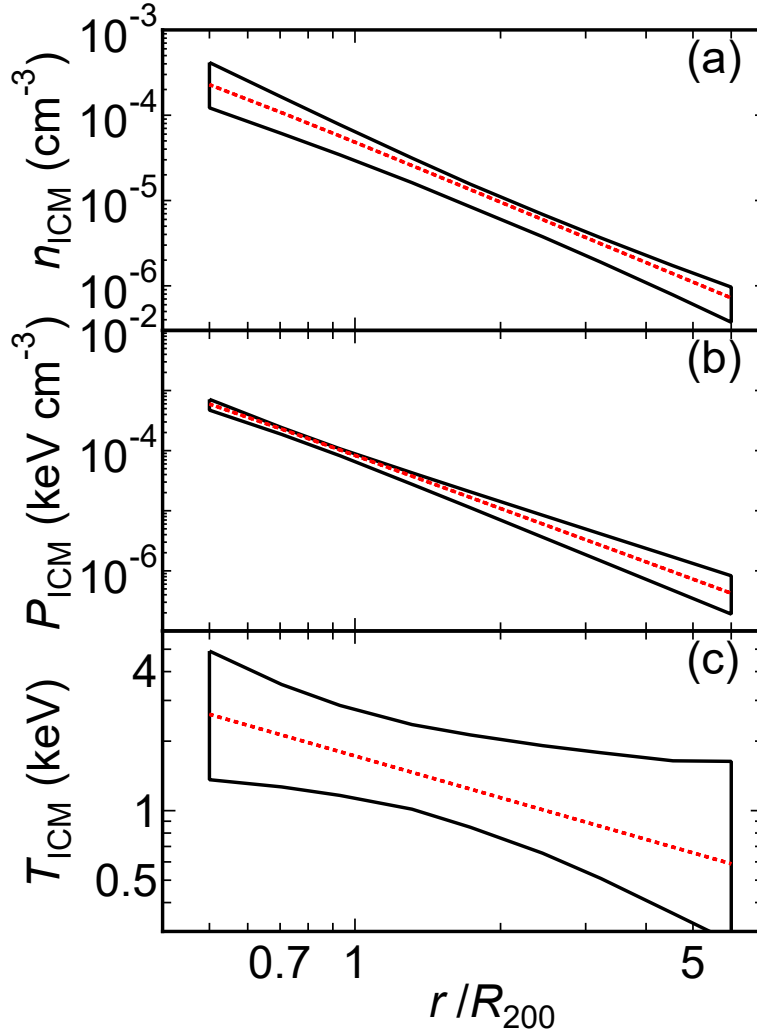


Figure 3. Same as Fig. 2 but when $n_{\text{SKA}} = 5 \text{ events deg}^{-2}$. The normalization $\text{DM}_{\text{fit},0}$ is not fixed in the fits.

uncertainties of a factor of two. However, the power-law fit of the y data and thus the converted profile of pressure depend on the y signals available only at $\lesssim 1.5 R_{200}$ (Fig. 1). Thus, the obtained pressure profile for $\gtrsim 1.5 R_{200}$ is correct only when the profile can be represented by a power-law out to the outermost region. On the other hand, the power-law fit of the DM data depends not only on the inner region but also on the outer region, because FRBs observed in the outer region far outnumber those observed in the inner region although their DMs tend to be small (see Appendix and the similar lengths of the error bars or δDM_i in Fig. A1a). This means that the ICM density can actually be determined even at $r > 2 R_{200}$.

The detection rate of FRBs and the intrinsic dispersion of their DMs have large uncertainties at present. Thus, we consider the case where the detection rate is four times smaller or $n_{\text{SKA}} = 5 \text{ events deg}^{-2}$, which is equivalent to the case where the intrinsic dispersion is two times larger or $\sigma_{\text{DM}} = 2 \sigma_{\text{DM17}}$. The results are shown in Fig. 3; the errors become larger by a factor of $\lesssim 2$ than those in Fig. 2. One reason for the larger error is the small number of FRBs detected in the inner region, which leads to the large uncertainty of n_{ICM} at $r \sim r_{\text{min}} = 0.5 R_{200}$ (Fig. 3a). However, the ICM density may be estimated well at that radius with high spatial resolution SZ measurements such as MUSTANG-2⁴ and NIKA2⁵. Thus, we study the case where we fix the normalization $\text{DM}_{\text{fit},0} = \text{DM}_{\text{fit}}(\theta_{\text{min}})$ in equation (13) at the value given by the cluster model (section 3.1) and we vary only the index s . The results are shown in Fig. 4; the errors are much reduced compared with Fig. 3 especially at $r \sim R_{200}$. Note that n_{ICM} at $r_{\text{min}} = 0.5 R_{200}$

⁴ <http://www.gb.nrao.edu/mustang/>

⁵ <http://ipag.osug.fr/nika2/Welcome.html>

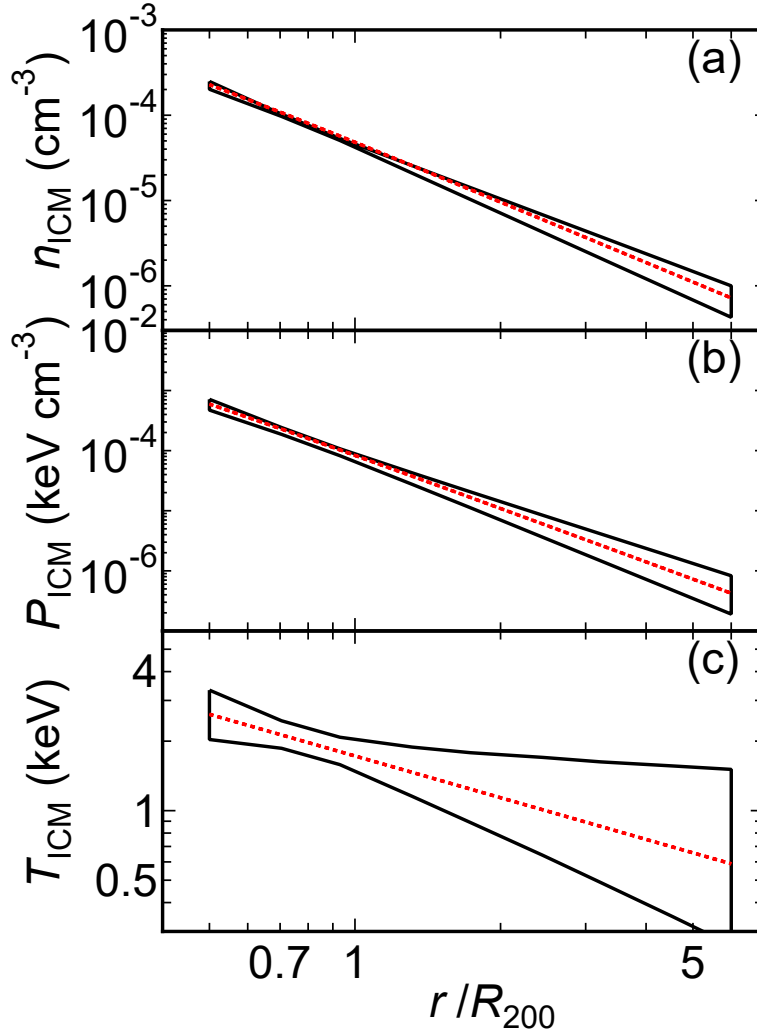


Figure 4. Same as Fig. 3 but when $DM_{\text{fit},0}$ is fixed in the fits.

slightly changes because the normalization of n_{ICM} depends on the index s (equation (14)).

FRBs may be affected by pulse broadening through scintillation. The pulse broadening by the IGM is expected to be negligible compared with that by the ISM of the Milky Way and the FRB’s host galaxy (Goodman 1997; Macquart & Koay 2013; Masui et al. 2015). If the turbulence that is responsible for the scintillation is a Kolmogorov type and the cutoff scale is the same, the strength of the broadening (scattering measure; SM) is proportional to $n_e^2 L_{\text{obj}}$, where L_{obj} is the depth of the intervening medium (e.g. ISM or ICM) along the line of sight (Goodman 1997; Macquart & Koay 2013). For the ICM, the SM is expected to be large in the inner region of the cluster. At $r \sim 0.5 R_{200} = 1.31$ Mpc, which is the innermost radius for our analysis, the density is $n_{\text{ICM}} \sim 2 \times 10^{-4} \text{ cm}^{-3}$ (Fig. 2) and the depth is $L_{\text{ICM}} \sim 1.31$ Mpc. For the ISM in the inner halo of the Milky Way, the density is $n_{\text{ISM}} \sim 0.02 \text{ cm}^{-3}$ and the depth is $L_{\text{ISM}} \sim 1$ kpc (e.g. Kataoka et al. 2015). Thus, the ratio of the SM is

$$\frac{SM_{\text{ICM}}}{SM_{\text{ISM}}} = \frac{n_{\text{ICM}}^2 L_{\text{ICM}}}{n_{\text{ISM}}^2 L_{\text{ISM}}} \sim 0.1. \quad (19)$$

This means that the SM associated with the ICM probably is smaller than that associated with the ISM. Considering the fact that the latter has inevitably been affecting the pulses of FRBs, the effects of the former is probably not serious for the detectability of the FRBs. Moreover, SM_{ICM} becomes even smaller if the cutoff scale of the turbulence is larger (equations (30) and (31) in Macquart & Koay 2013), which is likely given the large size of clusters of galaxies.

4. DISCUSSION

We have proposed a new method to observe the ICM including WHIM in the outskirts of galaxy clusters. In this method, DMs of numerous FRBs and the SZ effect are combined. Since the DMs and the SZ effect give information on the ICM density and pressure, respectively, we can estimate the temperature of the ICM from them. From mock observations of a massive cluster with SKA1-MID and *Planck*, we showed that the ICM density could be determined even at $> 2 R_{200}$, while the temperature profile could be derived out to $\sim 1.5 R_{200}$, and this maximum radius is limited by the current sensitivity of the SZ observations (Planck Collaboration et al. 2013a,b). We find that the low- ℓ excess ($\ell \lesssim 50$) in the *Planck* noise power spectrum $P_{\ell, \text{noise}}$ due to residual foreground contamination (Planck Collaboration et al. 2015b) has a non-negligible impact on the simulated y errors in the cluster outskirts. Hence, it will be important in cluster outskirt studies to reduce the level of foreground contamination in y maps at large angular scales.

The combination of our method and X-ray observations can be useful. For example, clumpiness of the ICM could be studied. The ICM density and temperature have been obtained for the interior ($\lesssim R_{200}$) of many clusters especially with *Suzaku* (e.g. Reiprich et al. 2013). The X-ray surface brightness of a cluster is represented by

$$S_X \propto \int_{-\infty}^{\infty} n_{\text{ICM}}^2 dL, \quad (20)$$

if the weak temperature dependence is ignored. The density dependence (n_{ICM}^2) is different from that for the DM (n_{ICM}) in equation (4). This means that if the ICM is moderately clumpy on a small scale that cannot be resolved by X-ray telescopes, S_X will be higher than that for smoothly distributed ICM with the same mass. This does not happen for the DM, which is not dependent on the clumpiness for a given column density. Thus, n_{ICM} determined by X-ray observations is systematically higher than that determined by DM observations. Note that while the y parameter depends linearly on n_{ICM} as does the DM (equation (10)), its behavior may be different from that of the DM. For example, if the clump size is relatively large and the ICM is in pressure equilibrium on that scale, the DM values depend on whether the line-of-sight to a FRB crosses one or more clumps because the column density fluctuates, while the y parameter is not much affected by the clumping.

The large-scale structure filaments that connect clusters are also expected to have the WHIM (Cen & Ostriker 1999), although it is difficult to detect the SZ effect toward them because they are usually located at $r \gg R_{200}$. However, the typical density of a particular filament can be obtained if a sufficient number of FRBs are detected toward the filament and their DMs are measured. Here the location of the filament can be inferred from galaxy distributions. One problem is that the density n_{fil} is degenerate with the depth of the filament along the line of sight L_{fil} , because $\text{DM}_{\text{fil}} \propto n_{\text{fil}} L_{\text{fil}}$ assuming that n_{fil} is constant. However, this degeneracy can be resolved by an observation of line emissions from the filament. For example, the WHIM is expected to radiate OVII and OVIII line emissions (Yoshikawa et al. 2003), and the line surface brightness varies as $S_L \propto n_{\text{fil}}^2 L_{\text{fil}}$. Thus, the density can be derived as $n_{\text{fil}} \propto S_L / \text{DM}_{\text{fil}}$. The oxygen lines could be observed with *DIOS* (Ohashi et al. 2015) and *Athena*⁶ in the future.

In the future, the efficiency of FRB searches may dramatically improve. If FRBs are found to be bright at lower frequencies, they can be detected with SKA1-LOW, which has a huge FOV (20.77 deg^{-2} at 110 MHz; Dewdney et al. 2016). When SKA2 becomes available, the sensitivity will increase by a factor of 10 compared with SKA1⁷, which means that the required exposure time will be significantly reduced. Moreover, if the origin of the dispersion, σ_{DM}^2 , is revealed, its influence on the error, $\delta(\text{DM})_{\text{ICM}}$ (equation (8)), can be decreased by considering an appropriate correction based on this knowledge. For example, if the DMs of FRBs vary with the distance and the positions of the hosts are known well enough to get a redshift, the distance dependence can be removed. This could greatly reduce the uncertainty of the DM values, and make the errors in our method much smaller. Although we have focused on individual cluster measurements, this method can be readily generalized to study a stacked ensemble of high-redshift clusters or group-sized systems. The Canadian Hydrogen Intensity Mapping Experiment⁸ and The Next Generation Very Large Array⁹ may also be useful for this study.

We thank Ue-Li Pen for useful discussion. This work was supported by KAKENHI No. 15K05080 (YF), 15H03639 (TA), and 15K17614 (TA). KU acknowledges support from the Ministry of Science and Technology of Taiwan through grants MOST 103-2112-M-001-030-MY3 and MOST 103-2112-M-001-003-MY3. CLS was supported in part by Chandra

⁶ <http://www.the-athena-x-ray-observatory.eu/>

⁷ <http://astronomers.skatelescope.org/ska2/>

⁸ <http://chime.phas.ubc.ca/>

⁹ <https://science.nrao.edu/futures/ngvla>

grants GO5-16131X and GO5-16146X and NASA XMM-Newton grants NNX15AG26G and NNX16AH23G. KWW was partially supported by Chandra grants GO5-16125X, GO6-17108X, and NASA ADAP grant NNH16CP10C.

APPENDIX

A. BACKWARD MODELING

In contrast with forward modeling (section 3.2), backward modeling does not require an ICM model for fits. However, it has a drawback that we need to use a derivative of the data (see equations (A3) and (A5)), which can magnify noise in the data. Moreover, the errors of the ICM data in the inner region are affected by those in the outer region (see equations (A4) and (A6)), which may complicate the comparison between the data and a model. However, it is instructive to compare the results of the backward modeling with those of the forward modeling when the ICM profile is rather smooth and the data have less noise.

A.1. Abel transform for radial ICM profiles

We assume that clusters are spherically symmetric for the sake of simplicity. Observable quantities for clusters are often written in the form of an integration along the line of sight (L):

$$f(\theta) = \int_{-\infty}^{\infty} g(L) dL = 2 \int_{d_A \theta}^{\infty} g(r) \frac{r dr}{\sqrt{r^2 - d_A^2 \theta^2}}, \quad (\text{A1})$$

where θ is the angle from the cluster center projected on the sky, r is the three-dimensional distance from the cluster center, and d_A is the angular diameter distance to the cluster. Using the Abel transform, equation (A1) is converted to be

$$g(r) = -\frac{1}{\pi d_A} \int_{r/d_A}^{\infty} \frac{df(\theta)}{d\theta} \frac{d\theta}{\sqrt{\theta^2 - r^2/d_A^2}} \quad (\text{A2})$$

(e.g. Yoshikawa & Suto 1999). In the case of the DM associated with a cluster, we take $f(\theta) = \text{DM}_{\text{ICM}}(\theta)$ and $g(r) = n_{\text{ICM}}(r)/(1+z)$ (equation (4)). Therefore,

$$n_{\text{ICM}}(r) = -\frac{1+z}{\pi d_A} \int_{r/d_A}^{\infty} \left[\frac{d}{d\theta} \text{DM}_{\text{ICM}}(\theta) \right] \frac{d\theta}{\sqrt{\theta^2 - r^2/d_A^2}}. \quad (\text{A3})$$

The integral in equation (A3) is numerically evaluated as

$$\sum_{i=i_{\text{obs}}}^{N-1} \frac{\text{DM}_{i+1} - \text{DM}_i}{\sqrt{\theta_{i+1/2}^2 - r^2/d_A^2}}, \quad (\text{A4})$$

where DM_i is the average DM of the i -th annulus bin, which corresponds to $\langle \text{DM} \rangle_{\text{ICM}}$ in section 2, and $\theta_{i+1/2} \approx \sqrt{\theta_i \theta_{i+1}}$ (Yoshikawa & Suto 1999). The typical angle of the i -th bin, θ_i , is the same as that in section 3.2. The index N is for the outermost bin and i_{obs} is for the bin corresponding to r/d_A .

Equation (10) indicates that by setting $f(\theta) = y(\theta)$ and $g(r) = \sigma_T P_{\text{ICM}}(r)/(m_e c^2)$ in equation (A2), we obtain

$$P_{\text{ICM}}(r) = -\frac{m_e c^2}{\pi d_A \sigma_T} \int_{r/d_A}^{\infty} \frac{dy(\theta)}{d\theta} \frac{d\theta}{\sqrt{\theta^2 - r^2/d_A^2}}. \quad (\text{A5})$$

The integral in equation (A5) is numerically evaluated as

$$\sum_{i=i_{\text{obs}}}^{N-1} \frac{y_{i+1} - y_i}{\sqrt{\theta_{i+1/2}^2 - r^2/d_A^2}}, \quad (\text{A6})$$

where y_i is the value of y in the i -th bin (equation (15)). Combining equations (A3) and (A5), we can obtain the temperature profile, $T_{\text{ICM}}(r) = P_{\text{ICM}}(r)/(k_B n_{\text{ICM}}(r))$.

A.2. Results

The model cluster we adopt here is the same as that in section 3.1 and we assume $n_{\text{SKA}} = 20 \text{ events deg}^{-2}$. As we did in the forward modeling in section 3.2, we consider four radial bins in logarithmically equal intervals ($N = 4$). We fix the outer boundary at $r_{\text{max}} = d_A \theta_{\text{max}} = 6 R_{200}$ and the inner boundary at $r_{\text{min}} = d_A \theta_{\text{min}} = 0.5 R_{200}$. The bins are common for DM and y . We calculate the assumed model profiles of $\text{DM}_{\text{ICM}}(\theta)$ and $y(\theta)$ using equations (4) and (10)

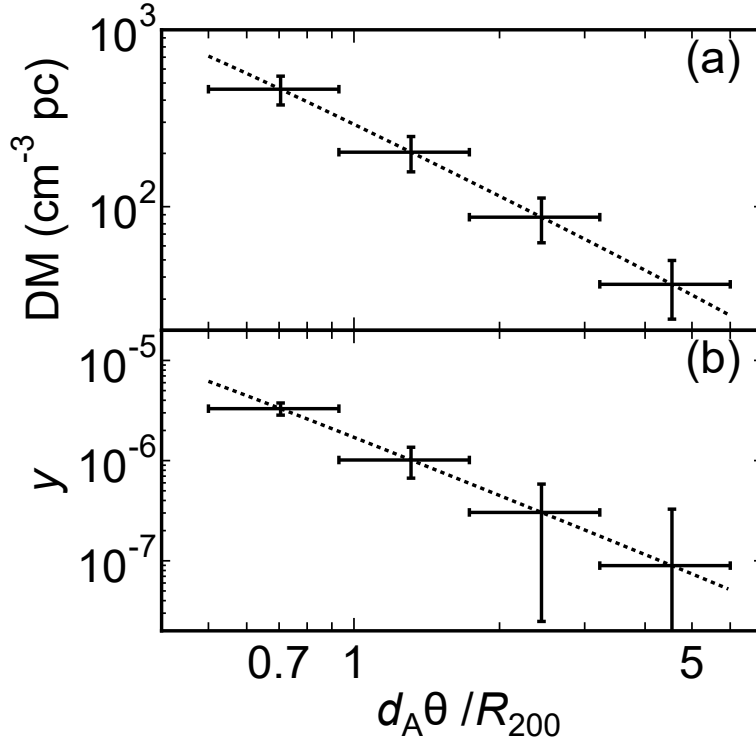


Figure A1. Original profiles of (a) the DM and (b) the y parameter when $n_{\text{SKA}} = 20 \text{ events deg}^{-2}$ are shown by the dotted lines. Horizontal error bars show the size of the bins. Vertical error bars are (a) $\sigma_{\text{DM}}/\sqrt{N_i}$ and (b) $\sigma_{y,i}$.

and the results are shown by the dotted lines in Fig. A1. We investigate whether the input density and temperature profiles are reproduced by the Abel transform (equations (A3) and (A5)). The results of the Abel transforms are shown in Fig. A2. The temperature of the ICM is given by $T_{\text{ICM}} = P_{\text{ICM}}/(n_{\text{ICM}}k_B)$. Uncertainties in the results were estimated using Monte Carlo simulations. At each annulus, the DM is randomly perturbed with a Gaussian distribution, with an amplitude determined by $\sigma_{\text{DM}}/\sqrt{N_i}$ (equation (8)), where $N_i = n_{\text{SKA}}S_i$ and S_i (deg^2) is the solid angle of the i -th bin. For the y parameter, we calculate simulated data with statistical errors, y_i , as we did in section 3.2. We obtained 10^3 different realizations. Fig. A2 shows that the input-model profiles are well reproduced by the mock observations. The ICM density is determined out to $r \sim 3 R_{200}$ with uncertainties of a factor of two, while the pressure and the temperature are determined out to $r \sim 1.5 R_{200}$. The large errors for the y parameter at $d_A\theta > 2 R_{200}$ (Fig. A1) limit the maximum radius for the determination of the pressure and temperature profiles. In Fig. A2, the centers of the crosses (reproduced quantities) do not necessary lie on the the dotted lines (input-model profiles), because we adopt relatively wide bins. Note that the number of the FRBs in the outermost bin in Fig. A1 ($d_A\theta \sim 3\text{--}6 R_{200}$) is ~ 480 . This means that the number of FRBs needed to derive the background dispersion measure, $\langle \text{DM} \rangle_{\text{out}}$, must be $N_{\text{out}} \gg 480$, if one wants to derive the profiles out to this radius (see section 2).

REFERENCES

- Akahori, T., Ryu, D., Kim, J., & Gaensler, B. M. 2013, *ApJ*, 767, 150
- Akahori, T., Ryu, D., & Gaensler, B. M. 2016, *ApJ*, 824, 105
- Akamatsu, H., Hoshino, A., Ishisaki, Y., et al. 2011, *PASJ*, 63, S1019
- Burke-Spolaor, S., & Bannister, K. W. 2014, *ApJ*, 792, 19
- Cen, R., & Ostriker, J. P. 1999, *ApJ*, 514, 1
- Champion, D. J., Petroff, E., Kramer, M., et al. 2016, *MNRAS*, in press
- Coward, D. M., Howell, E. J., Branchesi, M., et al. 2013, *MNRAS*, 432, 2141
- Danforth, C. W., & Shull, J. M. 2008, *ApJ*, 679, 194-219
- Davé, R., Cen, R., Ostriker, J. P., et al. 2001, *ApJ*, 552, 473
- Deng, W., & Zhang, B. 2014, *ApJL*, 783, L35
- Eckert, D., Molendi, S., Vazza, F., Ettori, S., & Paltani, S. 2013, *A&A*, 551, A22
- Fujita, Y., Ohira, Y., & Yamazaki, R. 2013, *ApJL*, 767, L4
- Fujita, Y., Tawa, N., Hayashida, K., et al. 2008, *PASJ*, 60, S343
- George, M. R., Fabian, A. C., Sanders, J. S., Young, A. J., & Russell, H. R. 2009, *MNRAS*, 395, 657
- Ghizzardi, S., Molendi, S., Pizzolato, F., & De Grandi, S. 2004, *ApJ*, 609, 638
- Goodman, J. 1997, *NewA*, 2, 449
- Han, J. L., van Straten, W., Lazio, T. J. W., et al. 2014, *AASKA14*, 041, <http://pos.sissa.it/cgi-bin/reader/conf.cgi?confid=215>

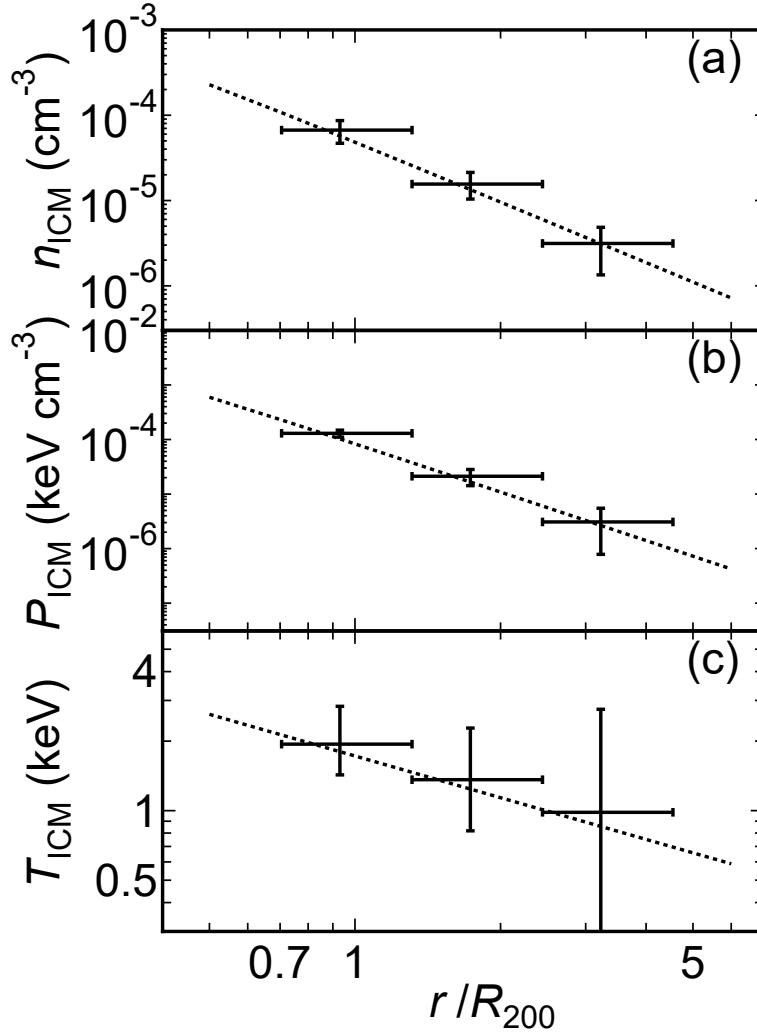


Figure A2. Crosses are reproduced profiles of (a) the ICM density and (b) the temperature. Input-model profiles (equations (11) and (12)) are shown by dotted lines.

Hoshino, A., Henry, J. P., Sato, K., et al. 2010, PASJ, 62, 371
 Ichikawa, K., Matsushita, K., Okabe, N., et al. 2013, ApJ, 766, 90
 Ioka, K. 2003, ApJL, 598, L79
 Inoue, S. 2004, MNRAS, 348, 999
 Kataoka, J., Tahara, M., Totani, T., et al. 2015, ApJ, 807, 77
 Kawaharada, M., Okabe, N., Umetsu, K., et al. 2010, ApJ, 714, 423
 Keane, E. F., Stappers, B. W., Kramer, M., & Lyne, A. G. 2012, MNRAS, 425, L71
 Keane, E. F., Johnston, S., Bhandari, S., et al. 2016, Nature, 530, 453
 Lorimer, D. R., Bailes, M., McLaughlin, M. A., Narkevic, D. J., & Crawford, F. 2007, Science, 318, 777
 Macquart, J. P., Keane, E., Grainge, K., et al. 2014, AASKA14, 055, <http://pos.sissa.it/cgi-bin/reader/conf.cgi?confid=215>
 Macquart, J.-P., & Koay, J. Y. 2013, ApJ, 776, 125
 Masui, K., Lin, H.-H., Sievers, J., et al. 2015, Nature, 528, 523
 Navarro, J. F., Frenk, C. S., & White, S. D. M. 1996, ApJ, 462, 563
 Nicastro, F., Mathur, S., Elvis, M., et al. 2005, Nature, 433, 495
 Ohashi, T., Ishisaki, Y., Ezoe, Y., et al. 2015, arXiv:1503.08405
 Petroff, E., Bailes, M., Barr, E. D., et al. 2015, MNRAS, 447, 246
 Planck Collaboration, Ade, P. A. R., Aghanim, N., et al. 2013a, A&A, 550, A131

Planck Collaboration, Ade, P. A. R., Aghanim, N., et al. 2013b, A&A, 554, A140
 Planck Collaboration, Ade, P. A. R., Aghanim, N., et al. 2015a, arXiv:1511.05156
 Planck Collaboration, Aghanim, N., Arnaud, M., et al. 2015b, arXiv:1502.01596
 Ravi, V., Shannon, R. M., & Jameson, A. 2015, ApJL, 799, L5
 Ryu, D., Kang, H., Hallman, E., & Jones, T. W. 2003, ApJ, 593, 599
 Reiprich, T. H., Basu, K., Ettori, S., et al. 2013, SSRv, 177, 195
 Reiprich, T. H., & Bhringer, H. 2002, ApJ, 567, 716
 Reiprich, T. H., Hudson, D. S., Zhang, Y.-Y., et al. 2009, A&A, 501, 899
 Sato, T., Sasaki, T., Matsushita, K., et al. 2012, PASJ, 64,
 Simionescu, A., Allen, S. W., Mantz, A., et al. 2011, Science, 331, 1576
 Spitler, L. G., Cordes, J. M., Hessels, J. W. T., et al. 2014, ApJ, 790, 101
 Sunyaev, R. A., & Zeldovich, Y. B. 1972, Comments on Astrophysics and Space Physics, 4, 173
 Takei, Y., Ohashi, T., Henry, J. P., et al. 2007, PASJ, 59, 339
 Thornton, D., Stappers, B., Bailes, M., et al. 2013, Science, 341, 53

- Tripp, T. M., Sembach, K. R., Bowen, D. V., et al. 2008, *ApJS*, 177, 39-102
- Dewdney, P., Turner, W., Braun, R., Santander-Vela, J., Waterson, M., Tan, G.-H. 2016, SKA1 System Baseline Design V2, Document number SKA-TEL-SKO-0000002 Revision 03, <http://astronomers.skatelescope.org/documents/>
- Umetsu, K., Broadhurst, T., Zitrin, A., et al. 2011, *ApJ*, 738, 41
- Umetsu, K., Medezinski, E., Broadhurst, T., et al. 2010, *ApJ*, 714, 1470
- Urban, O., Werner, N., Simionescu, A., Allen, S. W., Böhringer, H. 2011, *MNRAS*, 414, 2101
- Vikhlinin, A., Kravtsov, A., Forman, W., et al. 2006, *ApJ*, 640, 691
- Voit, G. M., Kay, S. T., & Bryan, G. L. 2005, *MNRAS*, 364, 909
- Walker, S. A., Fabian, A. C., Sanders, J. S., George, M. R., & Tawara, Y. 2012, *MNRAS*, 422, 3503
- Wong, K.-W., Irwin, J. A., Wik, D. R., et al. 2016, *ApJ*, 829, 49
- Wong, K.-W., & Sarazin, C. L. 2009, *ApJ*, 707, 1141
- Yoshikawa, K., & Suto, Y. 1999, *ApJ*, 513, 549
- Yoshikawa, K., Yamasaki, N. Y., Suto, Y., et al. 2003, *PASJ*, 55, 879